Earth and Planetary Science Letters 587 (2022) 117551

Contents lists available at ScienceDirect

Earth and Planetary Science Letters

www.elsevier.com/locate/epsl

Global Hg cycle over Ediacaran–Cambrian transition and its implications for environmental and biological evolution

Yaowen Wu [a,b], Runsheng Yin [c], Chao Li [d,e], Di Chen [c], Stephen E. Grasby [f], Tengfei Li [a,b], Sui Ji [a,b], Hui Tian [a,b,*], Ping'an Peng [a,b]

[a] State Key Laboratory of Organic Geochemistry, Guangzhou Institute of Geochemistry, Chinese Academy of Sciences, Guangzhou 510640, China
[b] CAS Center for Excellence in Deep Earth Science, Guangzhou 510640, China
[c] State Key Laboratory of Ore Deposit Geochemistry, Institute of Geochemistry, Chinese Academy of Sciences, Guiyang 550081, China
[d] State Key Laboratory of Oil and Gas Reservoir Geology and Exploitation & Institute of Sedimentary Geology, Chengdu University of Technology, Chengdu 610059, China
[e] State Key Laboratory of Biogeology and Environmental Geology, China University of Geosciences, Wuhan 430074, China
[f] Geological Survey of Canada, Natural Resources Canada, 3303 33rd Street NW, Calgary, Alberta T2L 2A7, Canada

ARTICLE INFO

Article history:
Received 18 September 2021
Received in revised form 2 April 2022
Accepted 13 April 2022
Available online 22 April 2022
Editor: B. Wing

Keywords:
Cambrian Explosion
mercury cycle
volcanism
OM burial
black shale

ABSTRACT

The Ediacaran–Cambrian (E–C) transition witnessed remarkable environmental changes, the extinction of the Ediacaran biota, and subsequent rapid diversification of Cambrian animals. However, the linkages between environmental and biological evolution are still under debate at this critical time. Here, we present new Hg abundance and Hg isotopes in sediments from South China, which are then combined with those published from the Indian craton to explore the co-evolution of environment and complex life during the E–C transition. In both areas, high Hg/TOC ratios and near-zero Δ^{199}Hg of the Late Ediacaran sediments suggest enhanced volcanism, whereas relatively high Hg/TOC ratios and positive Δ^{199}Hg shift upsection indicate volcanic-sourced atmospheric Hg(II) deposition in the earliest Cambrian. The dramatically decreasing Hg/TOC ratios and positive Δ^{199}Hg of early Cambrian Age 2 to 3 sediments indicate scavenging of dissolved seawater Hg(II) by organic matter particulates. Our Hg results suggest volcanism may have likely played a significant role in the extinction of Ediacaran biota and global negative carbon excursions near the E–C boundary. Furthermore, our Hg data provides new evidence of extensive OM burial in the early Cambrian Age 2 to 3 oceans, leading to a rapid increase of Earth-surface O_2 levels that coincided with appearance of more complex large-body animals. Our study provides new insights of the global Hg cycle into the co-evolution of the environment and complex life at this critical time.

1. Introduction

The Ediacaran–Cambrian (E–C) transition witnessed remarkable environmental changes and biological evolution in Earth's history (e.g., Knoll and Carroll, 1999; Kimura and Watanabe, 2001). The Ediacaran biota (ca. 575–541 Ma) was characterized by a distinct group of complex tubular and frond-shaped organisms without modern analog (e.g., Xiao and Laflamme, 2009). They disappeared near the Precambrian–Cambrian boundary, and began to be replaced by the small shelly fossil assemblages (SSFAs) during the earliest Cambrian (Fortunian and Age 2; ~541–521 Ma; Zhu et al., 2006). Then, diversification of Cambrian life reached the peak with the appearance of most phyla of modern animals and modern-like marine ecosystems (e.g., Knoll and Carroll, 1999; Erwin et al., 2011), e.g., large-body Chengjiang Biota at Age 3 in South China (Zhu et al., 2006). These biological evolutions were generally considered to be linked to environmental changes across the E–C transition (e.g., Li et al., 2018). The extinction of Ediacaran biota associated with basal Cambrian negative carbon isotopic excursion (BACE; ca. 541 Ma) represent fundamental biotic and environmental changes (Zhu et al., 2006). Widespread oceanic anoxia has been invoked to account for disappearance of Ediacaran biota (e.g., Kimura and Watanabe, 2001). However, this inference is not consistent with significant oceanic oxygenation as evidenced by increasing geochemical data of this critical time (Lyons et al., 2014; Chen et al., 2015b), indicating that oceanic anoxia is not the sole mechanism of the Ediacaran biota crisis.

* Corresponding author at: State Key Laboratory of Organic Geochemistry, Guangzhou Institute of Geochemistry, Chinese Academy of Sciences, Guangzhou 510640, China.
E-mail address: tianhui@gig.ac.cn (H. Tian).

https://doi.org/10.1016/j.epsl.2022.117551
0012-821X/

Rising oxygen levels across the E–C transition (perhaps >10–25% of present atmospheric O_2 level (PAL); Lyons et al., 2014) are believed to have exceeded the requirement by high oxygen-demanding early complex animals (0.5–4% of PAL; Mills et al., 2014), thus an important factor of promoting Cambrian biodiversity. Although enhanced organic matter (OM) burial and efficient oxygenic photosynthesis of eukaryotic diversification have long been proposed to promote increased O_2 levels on Earth's surface (Lenton et al., 2014; Brocks et al., 2017), the triggers for significant E–C atmospheric-oceanic oxygenation remain uncertain. Long-term continental weathering and terrestrial nutrient input have been proposed to stimulate the rise of filter-feeding organisms that generated larger organic particles, favoring rapid OM sinking rates, enhanced burial, and thus O_2 accumulation (Li et al., 2018). Meanwhile, expansion of anoxic waters may also promote more efficient organic matter burial, thus contributing to rising O_2 levels at this critical time (He et al., 2019). These disparate mechanisms have distinct implications for how the E–C land-ocean-atmosphere system operated and need direct evidence to be resolved.

Mercury (Hg) isotopes have been recently used as a robust tool to trace large igneous province volcanism, ocean/atmospheric chemistry, and biological evolution events throughout Earth's history (e.g., Zheng et al., 2018; Grasby et al., 2019; Shen et al., 2019; Them et al., 2019; Zerkle et al., 2020). Large volcanic eruptions have been considered as the dominant source of Hg(0) to Earth's surface environment in pre-Anthropocene time (Grasby et al., 2019). The volcanic Hg(0) has a residence time of ~0.5–1 yr, allowing for long-distance transport and dispersal (Selin, 2009), and enters the ocean primarily through direct atmospheric deposition and/or terrestrial riverine runoff (Them et al., 2019). In the ocean, Hg is mainly fixed in modern and ancient marine sediments via the uptake of dissolved Hg by organic matter and sulfide particles (Shen et al., 2020). Hg mass-independent fractionation (Hg-MIF; reported as Δ^{199}Hg) occurs during photochemical processes, and Δ^{199}Hg values have been used to trace the Hg sources of either terrestrial runoff or atmospheric deposition (Blum et al., 2014; Yin et al., 2016; Grasby et al., 2019). In contrast, mass-dependent fractionation (Hg-MDF; reported as δ^{202}Hg) results from various physical, chemical, and biological processes (Blum et al., 2014), and potentially provides insights into the redox state of the paleo-ocean (Fan et al., 2020). Given the strong complexation of Hg with organic matter and sulfide in sediments, post-depositional influence on fractionation of sedimentary Hg isotopic signals is thought to be small (Blum et al., 2014; Zheng et al., 2018; Zerkle et al., 2020). Therefore, Hg concentrations and isotopic signals in ancient marine sediments have potential to provide constraints on sources and cycling of Hg over geological times (Zheng et al., 2018).

While there are a few reports of Hg concentrations and isotopic composition in early Cambrian black shales (Yin et al., 2017; Zhu et al., 2021), a complete Hg dataset across the E–C transition is still lacking. Although Liu et al. (2021) observed anomalously high Hg peaks and variations in Hg isotopes at the E–C boundary in the Indian Craton, and provided evidence of enhanced terrestrial Hg input, the significance of Hg data was not further assessed regarding the oceanic-atmospheric oxygenation. Here, we present a high-resolution Hg record across the E–C sedimentary rocks in South China Craton and interpret the results in combination with those from the Indian Craton (Liu et al., 2021) in order to (1) reconstruct the evolution of global Hg cycle, and (2) explore the linkage between environmental changes and biological evolution at this critical period.

2. Geological setting

During the E–C transition, South China was an isolated craton surrounded by an open ocean; while the Indian craton was located in Gondwana land and had a palaeogeographic affinity with South China craton (**Fig. 1A**, Merdith et al., 2021). The sedimentary facies of South China include shallow-water carbonate facies on the Yangtze platform, narrow intra-platform facies, and deepwater slope to basinal facies in southeastern region (**Fig. 1B**, Yeasmin et al., 2017). The relative sea-level began to gradually rise at the beginning of the Cambrian period, and reached the highest levels during Cambrian Age 2 to Age 3 (ca. 521 Ma; **Fig. 2**; Peng et al., 2012). As a consequence of global transgression, black shales were deposited throughout the Yangtze Block (Jin et al., 2016).

The regional biostratigraphy, radiometric ages, carbon isotope stratigraphy, and typical marker layers are integrated to establish the stratigraphic framework of the Ediacaran-Cambrian transitional successions (**Fig. 2**). The E–C boundary in South China is defined by the extinction of Ediacaran biota and the appearance of SSFAs in shallow shelf Meishucun and Xiaotan sections and the recognizable BACE (Fig. 2; Zhu et al., 2006). In the deepwater slope and basin regions, the Liuchapo Formation is considered to straddle across the E–C boundary, and two U–Pb ages of 542.1 ± 5.0 Ma and 542.6 ± 3.7 Ma obtained respectively from the Ganziping and Bahuang sections likely represent the E–C boundary (**Fig. 2**; Chen et al., 2015a). For the ZK4411 drillcore, the first negative excursion (N1) of $\delta^{13}C_{org}$ values (ca. −38‰; Wu et al., 2021) in the lower part of the Liuchapo Formation, most likely representing the E–C boundary, can be correlated with the similar negative carbon isotope excursions observed in the Liuchapo cherts at the Ganziping and Longbizui sections in the slope region and the basal Zhujiaqing Formation at Xiaotan section in the inner shelf region (**Fig. 2**; Cremonese et al., 2013; Chen et al., 2015a). The Ni-Mo polymetallic /V-rich marker layers and the third negative $\delta^{13}C_{org}$ excursions (N3) are well correlated between the shallow shelf and slope sections across the Yangtze Block. Re-Os ages of 521 ± 5 Ma and 520.3 ± 9.1 Ma have been obtained from these marker layers (Xu et al., 2011; Fu et al., 2016).

The studied ZK4411 drillcore from South China (28°02'32"N and 109°04'33"E, northeastern Guizhou Province) was located in a slope region of the Yangtze Block (**Fig. 1B**) and penetrates Doushantuo Formation Member IV (DST IV) of Late Ediacaran, Liuchapo Formation across the E–C boundary, and the Niutitang Formation of Cambrian Stage 2–3. The DST IV is mainly composed of OM-rich black shale (~8 m). The 45 m-thick Liuchapo Formation is dominated by cherts with thin layers of dolomite (~6 m) and organic-rich shale (~1 m) at its base. The overlying Niutitang Formation consists mainly of black shale (~60 m) and a thin layer of Ni–Mo marker layer (~0.5 m) at its base (**Figs. 2 and 3**). The biostratigraphy and sedimentary sequences of South China were also correlated with those of the Indian Craton (Jiang et al., 2003). The shallow water upper Dengying Formation and deepwater lower Liuchapo Formation in South China are equivalent to the D and E members of Ediacaran Krol Group in northern Indian, with a depositional age of ca. 550–539 Ma (Jiang et al., 2003). Based on the similar records of SSFAs (Zhu et al., 2006; Hughes, 2016), the upper Liuchapo/Zhujiaqing Formations in South China likely correspond to the cherty-phosphorites of the lower Tal Group of early Cambrian age in northern Indian (**Fig. 4**). As a result of globally recognized transgression during the late Cambrian Age 2, the widespread black shales were developed in both South China and Indian Cratons, which are respectively named as the Niutitang Formation and the lower Tal Group (Jiang et al., 2003; Jin et al., 2016).

To establish a stratigraphic correlation framework between South China and Indian Craton across the E–C transition, four stratigraphic intervals (I to IV) are divided based on biostratigraphy and sedimentary sequences, representing major stages of environmental changes and biological evolution. Interval I extends from the base of DST IV to E-C boundary, characterized by the

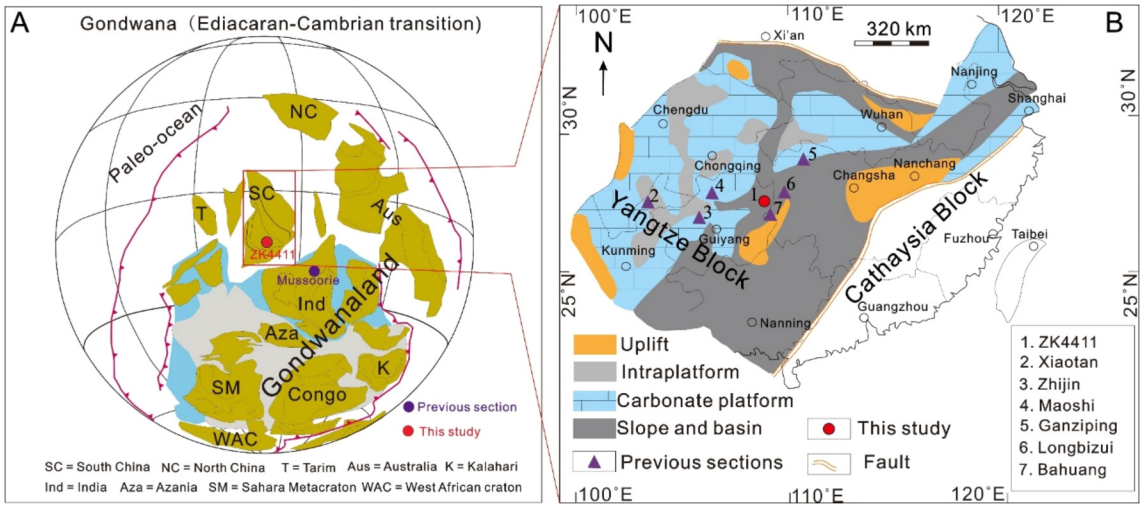

Fig. 1. (A) Paleogeography of Gondwanaland during the E–C transition showing the locations of the ZK4411 drillcore, South China and the Mussoorie section, Indian Craton (modified from Merdith et al., 2021). (B) Paleogeography of South China during the E–C transition showing sedimentary facies and the locations of previous sections and ZK4411 drillcore (after Yeasmin et al., 2017). (For interpretation of the colors in the figure(s), the reader is referred to the web version of this article.)

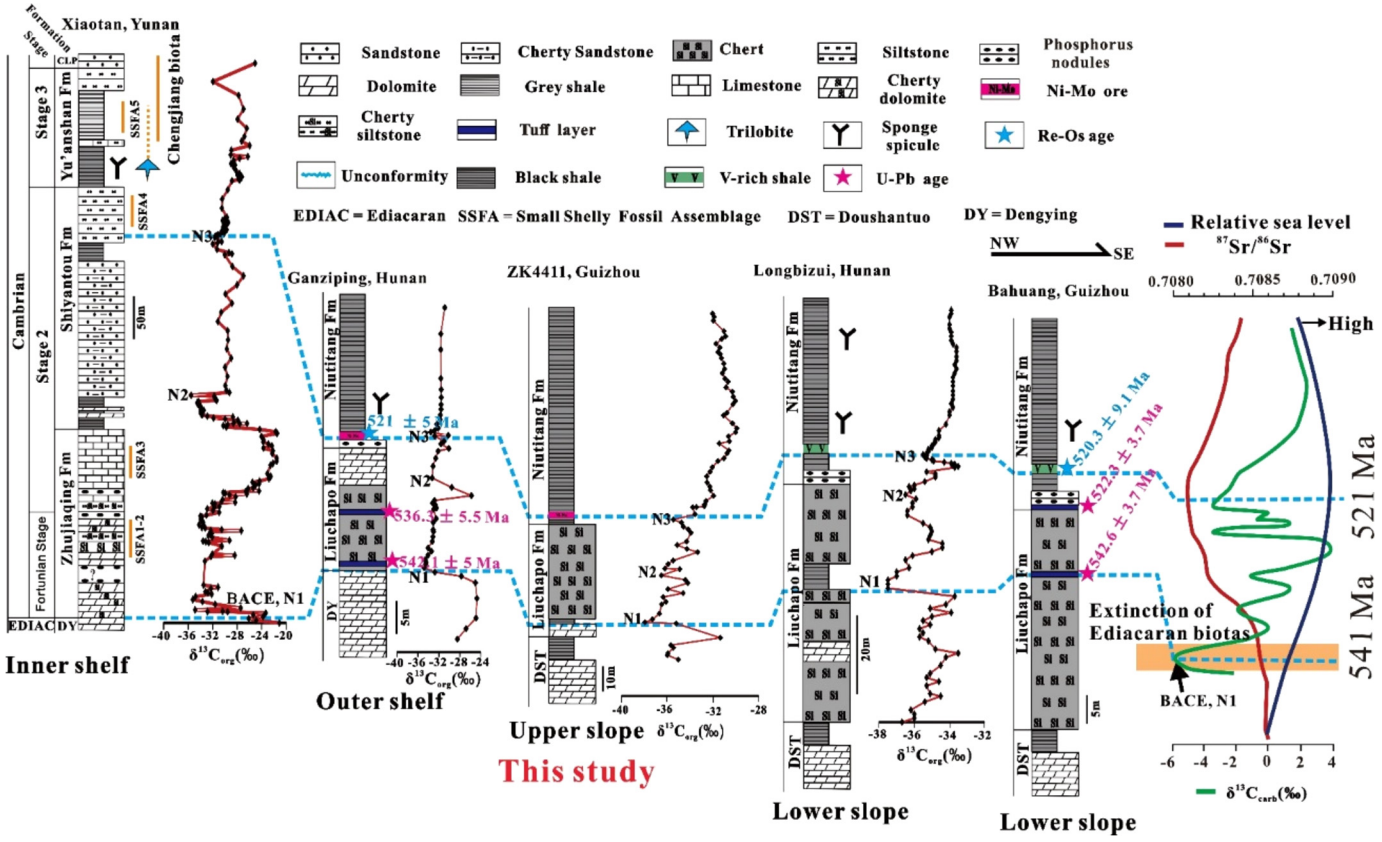

Fig. 2. Stratigraphic correlation across the Yangtze Block of South China from inner shelf to lower slope regions. Locations of these typical sections are shown in **Fig. 1**. 1: Xiaotan section (Cremonese et al., 2013; Jin et al., 2016); 2: Ganziping section (Chen et al., 2015a); 3: ZK4411 (this study); 4: Longbizui section (Guo et al., 2013); 5: Bahuang section (Chen et al., 2015a). The organic carbon isotope ($\delta^{13}C_{org}$) of ZK4411 drillcore are referenced from Wu et al. (2021). Re-Os ages for Ni-Mo marker layer of Ganziping section and V-rich layer of Bahuang section are from Xu et al. (2011) and Fu et al. (2016), respectively; U–Pb ages for Ganziping and Bahuang sections are from Chen et al. (2015a). The distribution of bio-fossil records is from Jin et al. (2016) and reference therein. The $^{87}Sr/^{86}Sr$ curve and relative sea level changes are from Peng et al. (2012) and reference therein. The $\delta^{13}C_{carb}$ curve is referenced from Zhu et al. (2006).

extinction of Ediacaran biota. Interval II is based on BACE and appearance of SSFAs during Cambrian Fortunian to Age 2, and Interval III mainly consists of widespread black shales formed under globally recognized transgression during Cambrian Age 2–3. Interval IV is marked by large-body Chengjiang Biota during Cambrian early to middle Age 3 (**Figs. 3 and 4**).

3. Samples and methods

3.1. Samples

Total sulfur (TS), Hg concentrations and isotopes were measured on forty-eight fresh core samples of ZK4411 drillcore covering the

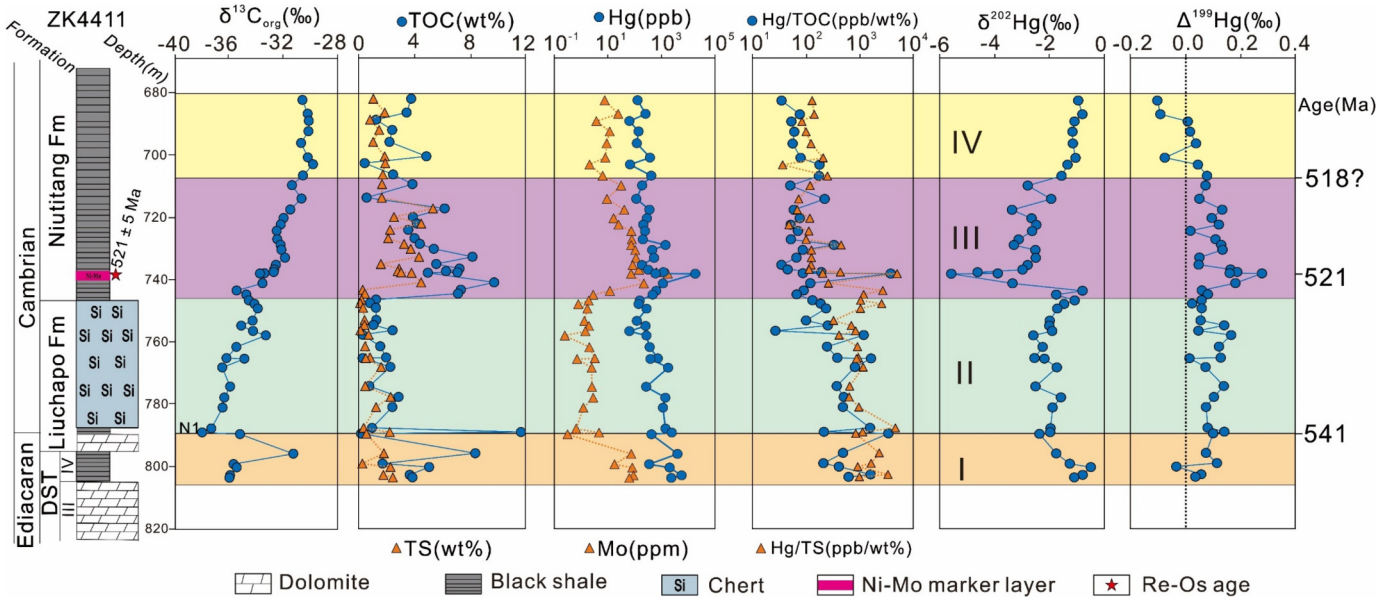

Fig. 3. Stratigraphic profiles of Hg concentrations, isotope compositions, and other related geochemical parameters for the E–C sediments in South China. Re-Os age for Ni-Mo marker layer is from Xu et al. (2011). The profiles of TOC, Mo and $\delta^{13}C_{org}$ are referenced from Wu et al. (2021).

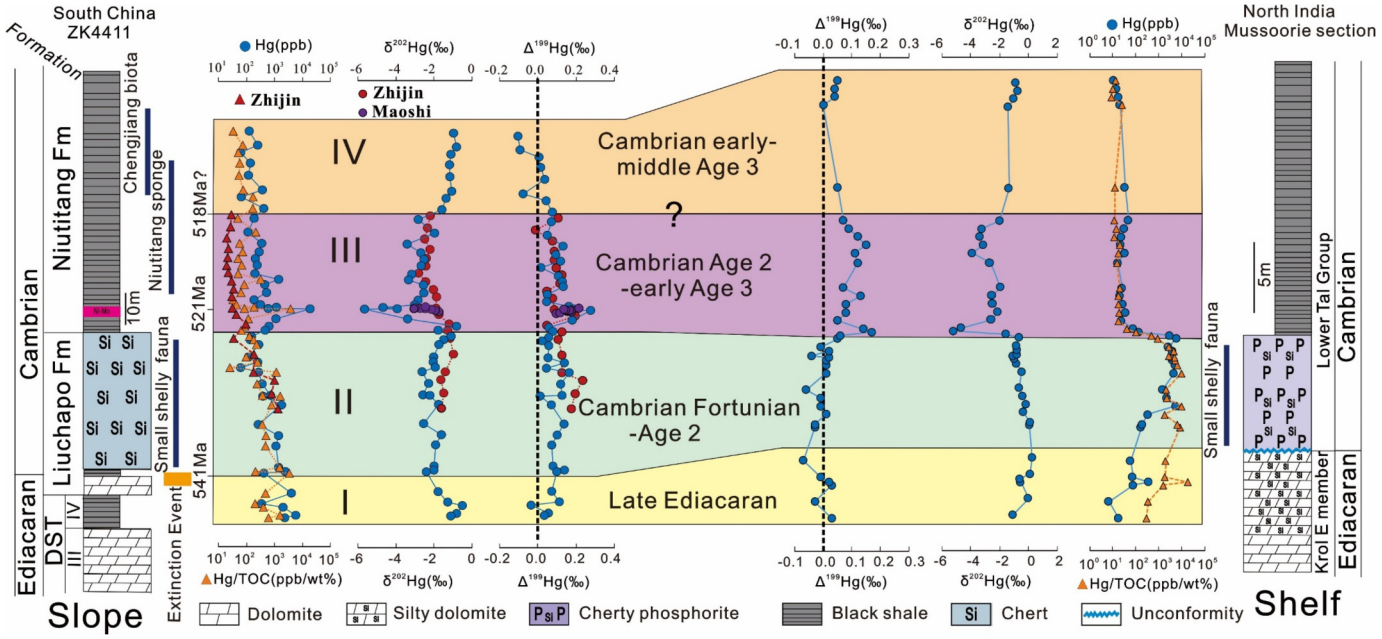

Fig. 4. Correlation of profiles for Hg concentrations and isotopes for E–C sediments in South China and the Indian craton. The data of the Mussoorie section in the Indian Craton are from Liu et al. (2021). The data of the Zhijin and Maoshi sections in South China are from Yin et al. (2017).

E-C transition whose total organic carbon contents (TOC), organic carbon isotopes ($\delta^{13}C_{org}$) and molybdenum (Mo) concentrations have been published in Wu et al. (2021). The bulk samples were ground into a 200 mesh size using an agate mortar and then preserved in a desiccator before instrumental analysis.

3.2. TS concentrations

Total sulfur contents were measured on both HCl-treated and non-treated samples using a Leco CS230 carbon/sulfur analyzer at the State Key Laboratory of Organic Geochemistry in Guangzhou Institute of Geochemistry, Chinese Academy of Sciences. In the HCl-treated case, the powdered samples (80–120 mg) were treated with 6 M HCl until carbonates have been removed thoroughly, then washed using deionized water, and dried at 60 °C overnight before instrumental analysis. The differences of TS contents between HCl-treated and non-treated samples are generally less than 0.3% (Supplemental **Table 1**), indicating that HCl-treatment used in some studies (e.g., Zhu et al., 2021) does not significantly affect the measurement of total sulfur content. Nevertheless, the TS contents measured on non-treated samples are used in this study.

3.3. Total Hg concentrations

Total Hg concentrations were determined using a Nippon MA-2 direct combustion system at the State Key Laboratory of Environmental Geochemistry, Chinese Academy of Sciences (CAS). The accuracy and precision of Hg concentrations were assessed by analyzing procedural blanks, standard reference materials (GSS-4, soil, n = 10, 590 ppb) and sample duplicates. Generally, measurements

of standard reference material showed recoveries of 90–110%, and measurement errors for triplicate analyses were <8%.

3.4. Hg isotopes analysis

A double-stage tube furnace coupled with 10 mL of 40% mixed acid solutions ($HNO_3/HCl = 2/1$, v/v) were used for Hg pre-concentration, and this combustion method was developed and validated for Hg isotope analysis in an early study (Zerkle et al., 2020). For those samples with high Hg concentrations (>25 ng/g), an alternative acid digestion method using mixed acid solutions ($HNO_3/HCl = 1/3$, v/v) was used for Hg pre-concentration (Yin et al., 2017). After pre-concentration, all the solutions were diluted to ultimate acid concentration of ~20% with 10 mL of 18.2 MΩ•cm water, and then the diluted solutions were kept in a refrigerator at 2–4 °C before on-line test of Hg isotope. Hg isotopes were analyzed using a Neptune Plus multi-collector inductively coupled plasma mass spectrometry (Thermo Electron Corp, Bremen, Germany) at the State Key Laboratory of Environmental Geochemistry (Guiyang, China), Chinese Academy of Sciences, following the procedure described by Zerkle et al. (2020). NIST SRM 3133 Hg standard solutions with matrix and concentration similar to sample dilutions, were used for mass bias using standard-sample bracketing. Hg isotopes are reported as delta values (δ) in per mil (‰) referenced to the analyzed NIST SRM 3133 before and after each sample, following the convention of Blum and Bergquist (2007) with Equation (1):

$$\delta^{XXX}Hg(‰) = \left[\frac{\left(\frac{XXX_{Hg}}{198_{Hg}}\right)_{sample}}{\left(\frac{XXX_{Hg}}{198_{Hg}}\right)_{NIST\ SRM3133}} - 1 \right] \times 1000 \quad (1)$$

Mass-independent fractionation (MIF) is reported in Δ notation (Δ^{XXX} Hg), which describes the difference between the measured δ^{xxx}Hg and theoretically predicted δ^{xxx}Hg values, using Equation (2):

$$\Delta^{XXX}Hg\ (‰) = \delta^{XXX}Hg_{sample} - \beta \times \delta^{202}Hg_{sample} \quad (2)$$

where β values are 0.2520 for ^{199} Hg, 0.5024 for ^{200} Hg, and 0.7520 for ^{201} Hg, respectively. The overall average and uncertainty of NIST-3177 (δ^{202}Hg: -0.54 ± 0.10‰; Δ^{199}Hg: -0.02 ± 0.05‰; Δ^{201}Hg: -0.02 ± 0.05‰, 2SD, n = 3) and GSS-4 (δ^{202}Hg: -1.67 ± 0.14‰; Δ^{199}Hg: -0.36 ± 0.07‰; Δ^{201}Hg: -0.38 ± 0.08‰, 2SD, n = 3) agree well with previously published results (Blum and Bergquist, 2007). Analytical uncertainty was estimated based on the replication of the NIST-3177 standard solution, and the 2SD of NIST-3177 with δ^{202}Hg, Δ^{199}Hg, and Δ^{201}Hg of 0.10‰, 0.05‰ and 0.05‰, respectively, represent the analytical uncertainties of our samples.

4. Results

Measured TS, Hg concentrations and isotopic compositions as well as previously reported TOC and Mo concentrations for ZK4411 core samples are presented in Supplementary **Table 1**. As shown in **Fig. 3**, the TOC and TS concentrations range from 0.10 to 11.7 wt.% and 0.10 to 4.50 wt.%, respectively. Hg concentrations generally range from 64.0 to 5900 ppb, except extremely high value (19100 ppb) for the Ni-Mo marker layer at base of Interval III (738 m). From Interval I to middle part of Interval II (758–803 m), Hg/TOC ratios are high, fluctuating between 211 and 3490 ppb, and then decrease to 26.6–255 ppb in the upper part of Interval II (746–758 m). Upwardly, they display low levels (34.6–334 ppb) in Intervals III and IV (682–746 m), except for one abnormally high value (3850 ppb) at 738 m. Hg/TS ratios of Intervals I and II (746–803 m) are high (327–4700 ppb), and then decrease to 36.4–437 in intervals III and IV, except for one peak value (5070 ppb) at 738 m. δ^{202}Hg values are relatively high in Interval I, varying from −1.75 to −0.48‰, and then decrease to low values between −2.59 and −1.07‰. They continue to fall to lower levels in Interval III, from −0.79 to the lowest value of −5.61‰, and then upwardly increase from −1.56 to −0.79‰ in Interval IV. Interval I generally shows near-zero Δ^{199}Hg of −0.03 to +0.08‰, except for one high value of +0.12‰. Interval II shows relatively positive Δ^{199}Hg values, fluctuating between +0.02 and +0.17‰, and Interval III shows evidently positive Δ^{199}Hg values of +0.05 to +0.19‰, with a maximum value of +0.28‰ for the Ni-Mo marker layer at 738 m. Interval IV, however, largely shows near-zero Δ^{199}Hg values, ranging from −0.08 to +0.08‰.

The trends of Hg/TOC ratios and Hg isotopic compositions of ZK4411 drillcore are comparable to those of Zhijin and Maoshi sections in South China (**Fig. 4**). Moreover, the Hg/TOC ratios and Hg isotopic compositions of Intervals III and IV in South China are consistent with those of the Mussoorie section in Indian craton (**Fig. 4**; Liu et al., 2021). For Interval II, the Mussoorie section in Indian craton has stable high level of Hg/TOC ratios, near-zero Δ^{199}Hg, less negative δ^{202}Hg, whereas the sections of South China show decreasing Hg/TOC ratios, positive Δ^{199}Hg and negative δ^{202}Hg (**Fig. 4**).

5. Discussion

5.1. Volcanoes as a major source of Hg into the late Ediacaran and earliest Cambrian Oceans

The Intervals I and II samples of ZK4411 drillcore and Mussoorie section show no clear correlation between Hg and TOC because of excessive Hg decoupled from TOC (**Fig. 5A**). However, the Intervals III and IV black shale of both sites show a positive correlation between Hg and TOC ($r = 0.59, 0.85$; $p < 0.01$; respectively; **Fig. 5B**). In contrast, neither Intervals I and II nor Intervals III and IV of both South China and North Indian craton show obvious correlations between Hg and TS (**Fig. 5C**), e.g., only a weak correlation between Hg and TS ($r = 0.48, -0.23$; $p > 0.05$; **Fig. 5D**) for Intervals III and IV black shale. These results indicate the main host of Hg is organic matter rather than reduced sulfur, and normalization of Hg concentrations to TOC is appropriate to trace Hg sources in the present study.

Throughout geological history, volcanism was the predominant source of Hg to the environment, and the Hg was then cycled in the environment and eventually delivered to the ocean. In the ocean, Hg sinks to the seabed mostly through OM burial (Grasby et al., 2017). Over most geological periods, volcanic Hg emissions appear to be balanced by the OM sinks in the ocean. However, excessive Hg emissions by enhanced volcanism may result in anomalously high Hg/TOC ratios in marine sediments, which in turn can be used as a tracer of volcanic activity (Grasby et al., 2019). Notably, rapid transport of Hg-sulfides complexes to sediments in euxinic (H_2S-rich) conditions also leads to abnormally high Hg/TOC ratios of marine sediments (Shen et al., 2020). For example, the photic zone euxinia, a condition with H_2S-rich shallow waters, promotes the sequestration of atmospheric Hg(0) and photoreduction of S-bound Hg(II), and both processes lead to transfer of Hg-sulfides to sediments, resulting in abnormally high sedimentary Hg/TOC ratios (Zheng et al., 2018). However, the photic zone euxinia was not formed in E–C oceans and iron speciation data indicated oxic shallow waters overlying anoxic deep waters at this time (Li et al., 2010; Jin et al., 2016). Thus, the abnormally high

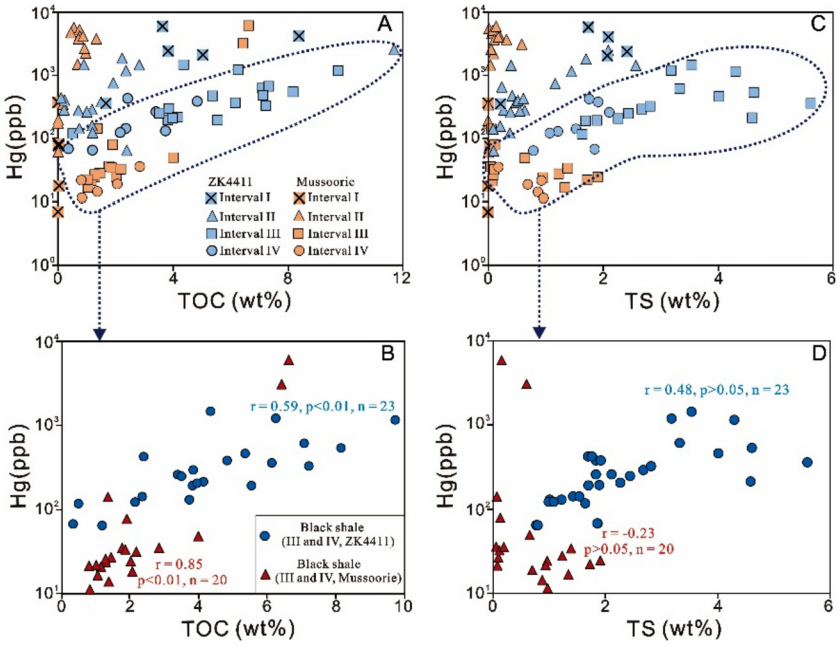

Fig. 5. The relationship between total Hg concentrations and TOC and TS contents. The samples with extremely high total Hg concentrations (ST162) are not included. The Hg, TOC, and TS concentrations of Indian Mussoorie section are from Liu et al. (2021).

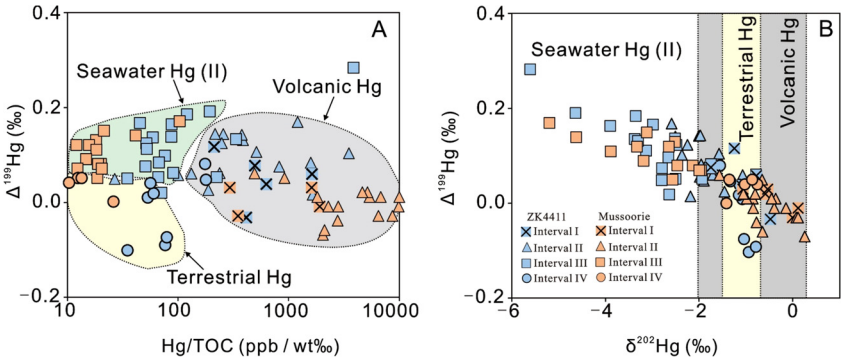

Fig. 6. The crossplots of Hg/TOC VS Δ^{199}Hg (A) and δ^{202}Hg VS Δ^{199}Hg (B) for the four Intervals (I to IV) of ZK4411 drillcore in South China (this study) and Mussoorie section in Indian Craton (Liu et al., 2021). The three Hg sources are interpreted in detail in the text. It is worthy to note that the boundaries of different Hg source are based on the data of current study. The range of volcanic Hg in Fig. B is based on Sial et al. (2021).

Hg/TOC ratios can be used to reflect volcanic Hg input in the present study.

Interval I and the lower to middle part of Interval II from ZK4411 core samples show high levels of Hg/TOC ratios (**Fig. 3**), implying large amounts of volcanic Hg input during late Ediacaran and earliest Cambrian. Similar high Hg/TOC ratios at the same intervals are also observed in the Mussoorie section of Indian craton (**Fig. 4**; Liu et al., 2021), further suggesting excessive Hg emissions by enhanced volcanism. Based on distribution of volcanic rocks, enhanced volcanism during the E-C transition have been inferred to occur in northern Indian Craton, West African craton, and Oman of Gondwanaland (Doblas et al., 2002; Bowring et al., 2007; Hughes et al., 2019). In addition, several thin tuff layers observed at the approximate E–C boundary in the Ganziping and Bahuang sections of South China may also indicate influence of frequent volcanic activities (**Fig. 2**; Chen et al., 2015a). The extensive volcanism during the late Ediacaran and earliest Cambrian may have been triggered by tectonic movement during Gondwana assembly (Doblas et al., 2002), and associated extensive volcanic Hg(0) emissions, through atmospheric transport, were settled into the oceans, and finally recorded in marine sediments of South China and India cratons (**Fig. 7A**).

Hg isotopes in sediments could provide constraints on sources of Hg (Grasby et al., 2019). The less negative δ^{202}Hg values (−1.09 to −0.48‰) and near-zero Δ^{199}Hg values (−0.03 to 0.06‰) from three ZK4411 core samples of lower Interval I in South China are comparable to those observed in Interval I of Mussoorie section (Liu et al., 2021). The range of δ^{202}Hg values in both sites is consistent with the volcanic Hg box (δ^{202}Hg = −2 to 0‰) proposed by Sial et al. (2021). The near-zero Δ^{199}Hg values at this time are also consistent with modern volcanic Hg(0) isotopic signals (Δ^{199}Hg =∼ 0‰; Zambardi et al., 2009). The high levels of Hg/TOC ratios combined with less negative δ^{202}Hg and near-zero Δ^{199}Hg values may jointly reflect enhanced volcanic Hg(0) input during late Ediacaran (**Fig. 6A and 6B**).

However, although relatively high Hg/TOC levels of upper Interval I and low-middle Interval II in ZK4411 drillcore of South China still suggest volcanic Hg input, positive Δ^{199}Hg values in South China (**Fig. 4**) are different from typical volcanic Hg(0) isotopic signals (Δ^{199}Hg =∼ 0‰; Zambardi et al., 2009). In contrast, high Hg concentrations and Hg/TOC ratios, as well as less negative δ^{202}Hg and near-zero Δ^{199}Hg values for the Interval II of the Mussoorie section, imply volcanic Hg(0) input and prolonged large volcanism effect near the Indian Craton of Gondwanaland (**Fig. 4**). The volcanic Hg(0) (Δ^{199}Hg =∼ 0‰) can be affected by photochemi-

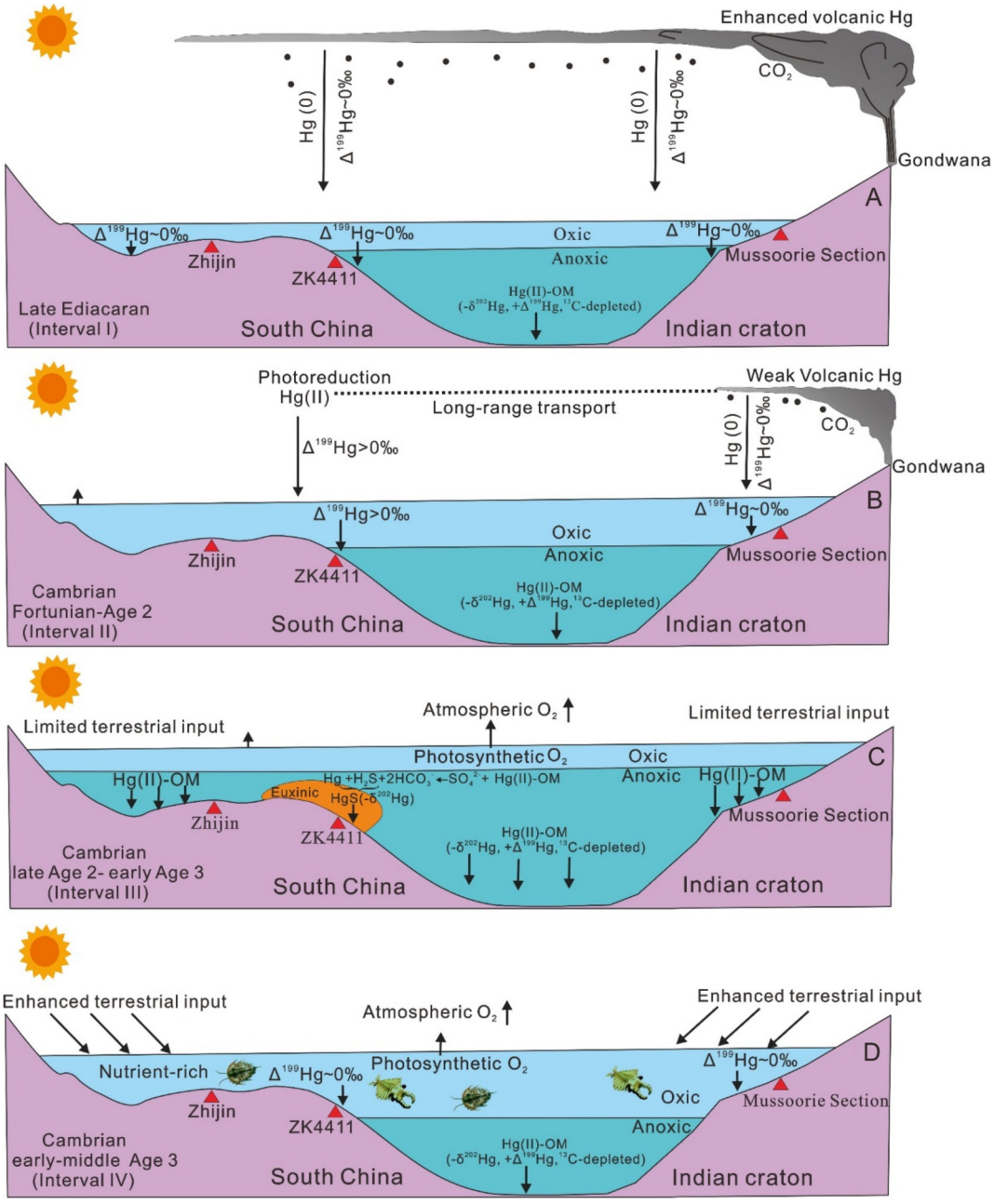

Fig. 7. Diagram showing the conceptual Hg cycles and redox states of the ocean during the E–C transition. A. Volcanic Hg as a major source of Hg in the Late Ediacaran and earliest Cambrian oceans; B. Weakening volcanism and volcanic-sourced atmospheric Hg (II) deposition in the earliest Cambrian ocean; C. Rapid removal of seawater Hg via OM burial in the Cambrian Ages 2–3 oceans; D. Terrestrial input of Hg into the oxic-expanding Cambrian Age 3 ocean.

cal processes during long distant transport. Hg(II) photoreduction results in positive Δ^{199}Hg in the atmospheric Hg(II) pool and negative Δ^{199}Hg in the gaseous Hg(0) pool (Bergquist and Blum, 2007). Seawater generally has Δ^{199}Hg values between +0.1‰ to +0.4‰ due to its dominant Hg source of atmospheric Hg (II) deposition (Štrok et al., 2015). As marine sediments scavenge Hg from seawater, they usually have positive Δ^{199}Hg values (Grasby et al., 2019). When the volcanism becomes weak, long-distance of Hg would result in the predominance of Hg(II) (positive Δ^{199}Hg) over the Hg(0) (Δ^{199}Hg∼0‰) deposition in marine sediments. Thus, the high Hg/TOC ratios and positive Δ^{199}Hg in South China may suggest volcanic-sourced atmospheric Hg(II) deposition through long-distance transport from Gondwanaland to South China, perhaps linked to weakening volcanism (**Fig. 7B**).

Notably, a dramatic decreasing trend of Hg/TOC ratios occurs in the upper part of Interval II in Zhijin and ZK4411 sections of South China (**Fig. 4**), implying remarkably reduced volcanic Hg input. However, high Hg/TOC ratios, as well as near-zero Δ^{199}Hg values for the Interval II of the Mussoorie section at the same time, still imply volcanic Hg(0) input. Therefore we infer that the volcanism at the time in the Gondwanaland was further weakened, and it only affected the areas near the Gondwanaland, such as Indian craton, but not South China.

5.2. Enhanced seawater Hg(II) deposition into Cambrian Age 2 to Age 3 Oceans

In Interval III of ZK4411, Zhijin and Mussoorie sites, Hg/TOC ratios stay at low levels compared to Intervals I and II (**Fig. 4 and**

6A), indicating continuously reduced volcanism in Gondwanaland at that time. Meanwhile, global transgression during Cambrian Age 2 may have caused the expansion of anoxic conditions, leading to an extensive OM sink and widespread formation of organic-rich black shales, such as those observed in the South China and India cratons (Jin et al., 2016; Liu et al., 2021). The OM sink can facilitate the removal of Hg from seawater to sediments (Grasby et al., 2019). The negative δ^{202}Hg and positive Δ^{199}Hg for the Interval III black shales in the Zhijin, Maoshi and ZK4411 sites of South China and Mussoorie section of Indian Craton (**Fig. 4 and 6B**) agree well with the results reported for modern seawater (δ^{202}Hg = −2.24‰ ± 0.58‰; Δ^{199}Hg = ∼ 0.2‰; Štrok et al., 2015). These similar Hg isotopic signals among different cratons may suggest large-scale seawater Hg (II) deposition into the Cambrian Age 2 to 3 ocean. In addition, positive correlations between Hg and TOC are observed in the Interval III black shales in South China and Indian cratons (**Fig. 5B**), suggesting scavenging of dissolved seawater Hg(II) by OM particulates. We therefore infer that a substantial amount of Hg in seawater was incorporated into sediments via large-scale OM burial during this period (**Fig. 7C**). Enhanced organic carbon burial in South China at that time is also supported by coupled positive shifts in $\delta^{13}C_{org}$ and $\delta^{13}C_{carb}$ (**Fig. 2**; Zhu et al., 2006).

It is worthy to note that extremely high Hg concentrations (19100 ppb), positive Δ^{199}Hg (+0.28‰), and most negative δ^{202}Hg (−5.6‰) concurrently occur in the Ni-Mo sulfide layer at the base of Niutitang Formation **(Fig. 3)**. The prominent Ni-Mo sulfide layers are thought to be formed under extremely euxinic water (H_2S-rich) conditions at a low sedimentary rate (Lehmann et al., 2007). In euxinic waters, seawater Hg(II) can be efficiently incorporated into sediments in the form of Hg-sulfide due to the strong affinity of Hg with reduced sulfur (Shen et al., 2020). Besides, our Hg results reveal that the volcanic-sourced atmospheric Hg(II) deposition into the earliest Cambrian Ocean of South China Craton, pushing seawater Hg(II) to high levels. H_2S-rich waters and high levels of seawater Hg(II) may jointly account for extremely high Hg concentration (19100 ppb) and positive Δ^{199}Hg (+0.28‰) in the Ni-Mo sulfide layers. The most negative δ^{202}Hg (−5.6‰) of the Ni-Mo sulfide layers is much lower than that of modern seawater (Štrok et al., 2015), which is likely related to the preferential absorption of isotopically light Hg during Hg-sulfide formation (Foucher et al., 2013).

5.3. Enhanced terrestrial Hg input into oxic-expanding Cambrian Age 3 oceans

Based on iron speciation data, a stepwise expansion of oxic surface waters for Cambrian Age 3 ocean has been proposed by Jin et al. (2016). The decreasing redox-sensitive Mo concentrations from Interval III to Interval IV also indicate less reducing bottom water condition (**Fig. 3**). In Interval IV of both the ZK4411 drillcore and Mussoorie section, Hg/TOC ratios remain low (**Fig. 6A**), suggesting only background volcanic Hg input during the Cambrian Age 3. Moreover, a negative shift of Δ^{199}Hg during this interval also indicates a dramatic change of Hg source into the ocean. The modern terrestrial Hg reservoir sourced from Hg(0) deposition is generally characterized by negative Δ^{199}Hg values with an average of −0.26‰ (Zheng et al., 2018). Fan et al. (2020) further proposed that before the emergence of land plants, the E–C terrestrial Hg reservoir may be more close to isotope compositions of silicate rocks (Δ^{199}Hg ∼ 0‰, δ^{202}Hg = −0.6‰ to −0.1‰). Therefore, the negative to near-zero Δ^{199}Hg and less negative δ^{202}Hg in Interval IV can be best explained by increased terrestrial material input (**Fig. 6B and 7D**). This inference is also consistent with enhanced continental weathering evidenced by increased $^{87}Sr/^{86}Sr$ ratios during this period (**Fig. 2**; Peng et al., 2012).

5.4. Implications for environmental and biological evolution during the E–C transition

Our Hg geochemistry results indicate enhanced volcanism during the late Ediacaran and earliest Cambrian, coinciding with the extinction of Ediacaran biota and BACE near the E–C boundary. Throughout Earth's history, large volcanism was generally linked to global extinction events, such as end-Triassic, Permian–Triassic and Late Ordovician mass extinctions (Thibodeau et al., 2016; Shen et al., 2019; Hu et al., 2020). Volcanic eruptions (e.g., sulphur and CO_2) may have contributed to global climatic perturbations, oceanic acidification, and ecosystem poisoning, thus resulting in collapse of marine ecosystem (Hu et al., 2020). Meanwhile, the large release of CO_2 contributes to carbon cycle perturbation, generating global negative carbon isotope excursions (Thibodeau et al., 2016), and may be a reasonable explanation for global BACE at the E–C boundary. Therefore, we consider that the enhanced volcanism may be a key factor of extinction of Ediacaran biota and BACE at the E–C boundary. In addition, large amounts of volcanic outgassing CO_2 into the atmosphere commonly generate greenhouse conditions, triggering global transgressions during the E–C transition (Doblas et al., 2002). This inference is also supported by a global sea-level rise during the earliest Cambrian (**Fig. 2**; Peng et al., 2012). However, the volcanism became weak as evidenced by a dramatic decreasing trend of Hg/TOC ratios and positive Δ^{199}Hg in South China from Fortunian to Age 2. The weakening volcanism and rising sea levels may reduce the effect of damage on marine ecosystem, contributing to recovery of ecosystem and appearance of SSFAs at this time. The sea level reached the highest level at Age 2 to Age 3, probably along with greenhouse effect, leading to the flooding of anoxic waters over continental shelves and slopes. The similar negative δ^{202}Hg and positive Δ^{199}Hg, as well as positive correlations of Hg and TOC in shelf and slope sections of South China and Indian Craton, provide new evidence of large-scale OM burial in a view of global oceanic system. Enhanced OM burial would have accelerated the net production of photosynthetic O_2 released to Earth's surface (Lenton et al., 2014; He et al., 2019), thus leading to a rapid increase in Earth-surface O_2 level at Age 3. The rising O_2 levels likely trigger the key innovations of the Cambrian metazoans from small shelly faunas to large-body, skeletonized animals at this critical time.

6. Conclusions

The integration of Hg/TOC and Δ^{199}Hg records from the ZK4411 drillcore (South China) and the Mussoorie section (North India) provides a snapshot of the global Hg cycle from the late Ediacaran to Cambrian Age 3. The high Hg/TOC ratios and near-zero Δ^{199}Hg records of Interval I suggest frequent large volcanism and volcanic-sourced Hg into the Late Ediacaran ocean. However, the similarly high Hg/TOC ratios but positive Δ^{199}Hg values for the lower and middle part of Interval II of ZK4411 drillcore in South China indicate volcanic-sourced atmospheric Hg(II) deposition through long-distance transport. Decreasing Hg/TOC ratios and positive Δ^{199}Hg values for the upper part of Interval II of ZK4411 drillcore in South China indicate weakening volcanism effect. The similarly low Hg/TOC ratios but positive Δ^{199}Hg values in Interval III of South China and Indian cratons then suggest removal of seawater Hg via large-scale OM burial in the Cambrian Age 2 to Age 3 oceans. The near-zero Δ^{199}Hg values for Interval IV of both sections reflect increased terrestrial Hg input into oxic-expanding Cambrian Age 3 oceans.

Enhanced volcanism during late Ediacaran as evidenced by our Hg results may have played a significant role in the extinction of Ediacaran biota and BACE near the E–C boundary. Meanwhile,

global transgression triggered by volcanic CO_2 emission and subsequent greenhouse effect may have contributed to the flooding of anoxic waters over continental shelves and slopes, favoring globally elevated OM burial at Age 3. At this critical time, enhanced OM burial promoted a rapid increase in O_2 released to Erath surface, likely triggering the rapid evolution of more complex large-body animals. Our study highlights the interaction between Erath's interior and surface processes and the necessity for understanding the co-evolution of environment and life in a view of Earth system.

CRediT authorship contribution statement

All the authors listed have made contributions to this work. **Y.W. Wu:** Investigation and Writing – Original Draft. **R.S. Yin:** Resources, Data Curation and Formal analysis. **C. Li:** Formal analysis and Funding acquisition. **D. Chen:** Data Curation. **S.E. Grasby:** Formal analysis. **T.F. Li:** Visualization. **S. Ji:** Visualization. **H. Tian:** Conceptualization, Writing – revised version, Supervision and Funding acquisition. **P.A. Peng:** Formal analysis.

Declaration of competing interest

The authors declare that they have no known competing financial interests or personal relationships that could have appeared to influence the work reported in this paper.

Acknowledgements

This study was jointly supported by the Natural Science Foundation of China (41925014, 41825019, 41821001 and 42130208) and the 111 Project of China (BP0820004). Prof. Boswell Wing and two anonymous reviewers are thanked for their comments and suggestion that have greatly enhanced the whole quality and clarity of this manuscript. This is contribution No.IS-3178 from GIGCAS.

Appendix A. Supplementary material

Supplementary material related to this article can be found online at https://doi.org/10.1016/j.epsl.2022.117551.

References

Bergquist, B.A., Blum, J.D., 2007. Mass-dependent and -independent fractionation of Hg isotopes by photoreduction in aquatic systems. Science 318, 417–420.
Blum, J.D., Bergquist, B.A., 2007. Reporting of variations in the natural isotopic composition of mercury. Anal. Bioanal. Chem. 388, 353–359.
Blum, J.D., Sherman, L.S., Johnson, M.W., 2014. Mercury isotopes in Earth and environmental sciences. Annu. Rev. Earth Planet. Sci. 42, 249–269.
Bowring, S.A., Grotzinger, J.P., Condon, D.J., Ramezani, J., Newall, M.J., Allen, P.A., 2007. Geochronologic constraints on the chronostratigraphic framework of the Neoproterozoic Huqf Supergroup, Sultanate of Oman. Am. J. Sci. 307, 1097–1145.
Brocks, J.J., Jarrett, A.J.M., Sirantoine, E., Hallmann, C., Hoshino, Y., Liyanage, T., 2017. The rise of algae in Cryogenian oceans and the emergence of animals. Nature 548, 578–581.
Chen, D., Zhou, X., Fu, Y., Wang, J., Yan, D., 2015a. New U-Pb zircon ages of the Ediacaran-Cambrian boundary strata in South China. Terra Nova 27, 62–68.
Chen, X., Ling, H.F., Vance, D., Shields-Zhou, G.A., Zhu, M., Poulton, S.W., Och, L.M., Jiang, S.Y., Li, D., Cremonese, L., Archer, C., 2015b. Rise to modern levels of ocean oxygenation coincided with the Cambrian radiation of animals. Nat. Commun. 6, 7142.
Cremonese, L., Shields-Zhou, G., Struck, U., Ling, H.-F., Och, L., Chen, X., Li, D., 2013. Marine biogeochemical cycling during the early Cambrian constrained by a nitrogen and organic carbon isotope study of the Xiaotan section, South China. Precambrian Res. 225, 148–165.
Doblas, M., Lopez-Ruiz, J., Cebria, J.M., Youbi, N., Degroote, E., 2002. Mantle insulation beneath the West African craton during the Precambrian–Cambrian transition. Geology 30, 839–842.
Erwin, D.H., Laflamme, M., Tweedt, S.M., Sperling, E.A., Pisani, D., Peterson, K.J., 2011. The Cambrian conundrum: early divergence and later ecological success in the early history of animals. Science 334, 1091–1097.
Fan, H.F., Fu, X.W., Ward, J.F., Yin, R.S., Wen, H.J., Feng, X.B., 2020. Mercury isotopes track the cause of carbon perturbations in the Ediacaran ocean. Geology 49, 248–252.
Foucher, D., Hintelmann, H., Al, T.A., MacQuarrie, K.T., 2013. Mercury isotope fractionation in waters and sediments of the Murray Brook mine watershed (New Brunswick, Canada): tracing mercury contamination and transformation. Chem. Geol. 336, 87–95.
Fu, Y., Dong, L., Li, C., Qu, W., Pei, H., Qiao, W., Shen, B., 2016. New Re-Os isotopic constrains on the formation of the metalliferous deposits of the Lower Cambrian Niutitang formation. J. Earth Sci. 27, 271–281.
Grasby, S.E., Shen, W., Yin, R., Gleason, J.D., Blum, J.D., Lepak, R.F., Hurley, J.P., Beauchamp, B., 2017. Isotopic signatures of mercury contamination in latest Permian oceans. Geology 45, 55–58.
Grasby, S.E., Them II, T.R., Chen, Z., Yin, R., Ardakani, O.H., 2019. Mercury as a proxy for volcanic emissions in the geologic record. Earth-Sci. Rev. 196, 102880.
Guo, Q., Strauss, H., Zhu, M., Zhang, J., Yang, X., Lu, M., Zhao, F., 2013. High resolution organic carbon isotope stratigraphy from a slope to basinal setting on the Yangtze Platform, South China: implications for the Ediacaran–Cambrian transition. Precambrian Res. 225, 209–217.
He, T.C., Zhu, M.Y., Mills, B.J.W., Wynn, P.M., Zhuravlev, A.Y., 2019, Tostevin, R., von Strandmann, P.A.E.P., Yang, A.H., Poulton, S.W., Shields, G.A. Possible links between extreme oxygen perturbations and the Cambrian radiation of animals. Nat. Geosci. 12, 468–474.
Hughes, N.C., 2016. The Cambrian palaeontological record of the Indian subcontinent. Earth-Sci. Rev. 159, 428–461.
Hughes, N.C., Myrow, P.M., Ghazi, S., McKenzie, N.R., Stockli, D.F., DiPietro, J.A., 2019. Cambrian geology of the salt range of Pakistan: linking the Himalayan margin to the Indian craton. Geol. Soc. Am. Bull. 131, 1095–1114.
Hu, D.P., Li, M.H., Zhang, X.L., Turchyn, A.V., Gong, Y.Z., Shen, Y.A., 2020. Large mass-independent sulphur isotope anomalies link stratospheric volcanism to the Late Ordovician mass extinction. Nat. Commun. 11, 2297.
Jiang, G.Q., Sohl, L.E., Christie-Blick, N., 2003. Neoproterozoic stratigraphic comparison of the Lesser Himalaya (India) and Yangtze block (south China): paleogeographic implications. Geology 31, 917–920.
Jin, C., Li, C., Algeo, T.J., Planavsky, N.J., Cui, H., Yang, X., Zhao, Y., Zhang, X., Xie, S., 2016. A highly redox-heterogeneous ocean in South China during the early Cambrian (~529–514 Ma): implications for biota-environment co-evolution. Earth Planet. Sci. Lett. 441, 38–51.
Kimura, H., Watanabe, Y., 2001. Oceanic anoxia at the Precambrian–Cambrian boundary. Geology 29, 995–998.
Knoll, A.H., Carroll, S.B., 1999. Early animal evolution: emerging views from comparative biology and geology. Science 284, 2129–2137.
Lyons, T.W., Reinhard, C.T., Planavsky, N.J., 2014. The rise of oxygen in Earth's early ocean and atmosphere. Nature 506, 307–315.
Lehmann, B., Nägler, T.F., Holland, H.D., Wille, M., Mao, J., Pan, J., Ma, D., Dulski, P., 2007. Highly metalliferous carbonaceous shale and Early Cambrian seawater. Geology 35, 403–406.
Lenton, T.M., Boyle, R.A., Poulton, S.W., Shields-Zhou, G.A., Butterfield, N.J., 2014. Co-evolution of eukaryotes and ocean oxygenation in the Neoproterozoic era. Nat. Geosci. 7, 257–265.
Li, C., Love, G.D., Lyons, T.W., Fike, D.A., Sessions, A.L., Chu, X., 2010. A stratified redox model for the Ediacaran ocean. Science 328, 80–83.
Li, C., Cheng, M., Zhu, M., Lyons, T.W., 2018. Heterogeneous and dynamic marine shelf oxygenation and coupled early animal evolution. Emerg. Top. Life Sci. 2, 279–288.
Liu, Z.R., Zhou, M.F., Wang, W., 2021. Mercury anomalies across the Ediacaran-Cambrian boundary: evidence for a causal link between continental erosion and biological evolution. Geochim. Cosmochim. Acta 304, 327–346.
Merdith, A.S., Williams, S.M.E., Collins, A.S., Tetley, M.G., Mulder, J.A., Blades, M.L., Young, A., Armistead, S.E., Cannon, J., Zahirovic, S., Muller, R.D., 2021. Extending full-plate tectonic models into deep time: linking the Neoproterozoic and the Phanerozoic. Earth-Sci. Rev. 214, 103477.
Mills, D.B., Ward, L.M., Jones, C., Sweeten, B., Forth, M., Treusch, A.H., Canfield, D.E., 2014. Oxygen requirements of the earliest animals. Proc. Natl. Acad. Sci. USA 111, 4168–4172.
Peng, S., Babcock, L.E., Cooper, R.A., 2012. The Cambrian period. In: Gradstein, F.M., Ogg, J.G., Schmitz, M.D., Ogg, G.M. (Eds.), The Geological Time Scale 2012, vol. 2. Elsevier, Amsterdam, pp. 437–488.
Sial, A.N., Chen, J.B., Korte, C., Pandit, M.K., Spangenberg, J.E., Silva-Tamayo, J.C., de Lacerda, L.D., Ferreira, V.P., Barbosa, J.N., Gaucher, C., Pereira, N.S., Riedel, P.R., 2021. Hg isotopes and enhanced Hg concentration in the Meishan and Guryul ravine successions: proxies for volcanism across the Permian-Triassic boundary. Front. Earth Sci. 9, 651224.
Selin, N.E., 2009. Global biogeochemical cycling of mercury: a review. Ann. Rev. Env. Resour. 34, 43–63.
Shen, J., Chen, J.B., Algeo, T.J., Yuan, S.L., Feng, Q.L., Yu, J.X., Zhou, L., O'Connell, B., Planavsky, N.J., 2019. Evidence for a prolonged Permian-Triassic extinction interval from global marine mercury records. Nat. Commun. 10, 1563.
Shen, J., Feng, Q.L., Algeo, T.J., Liu, J.L., Zhou, C.Y., Wei, W., Liu, J.S., Them, T.R., Gill, B.C., Chen, J.B., 2020. Sedimentary host phases of mercury (Hg) and implications for use of Hg as a volcanic proxy. Earth Planet. Sci. Lett. 543, 116333.

Štrok, M., Baya, P.A., Hintelmann, H., 2015. The mercury isotope composition of Arctic coastal seawater. C. R. Geosci. 347, 368–376.
Thibodeau, A.M., Ritterbush, K., Yager, J.A., West, A.J., Ibarra, Y., Bottjer, D.J., Berelson, W.M., Bergquist, B.A., Corsetti, F.A., 2016. Mercury anomalies and the timing of biotic recovery following the end-Triassic mass extinction. Nat. Commun. 7, 11147.
Them, T.R., Jagoe, C.H., Caruthers, A.H., Gill, B.C., Grasby, S.E., Grocke, D.R., Yin, R., Owens, J.D., 2019. Terrestrial sources as the primary delivery mechanism of mercury to the oceans across the Toarcian Oceanic Anoxic Event (Early Jurassic). Earth Planet. Sci. Lett. 507, 62–72.
Wu, Y., Tian, H., Li, J., Li, T., Ji, S., 2021. Reconstruction of oceanic redox structures during the Ediacaran-Cambrian transition in the Yangtze Block of South China: implications from Mo isotopes and trace elements. Precambrian Res. 359, 106181.
Xiao, S.H., Laflamme, M., 2009. On the eve of animal radiation: phylogeny, ecology and evolution of the Ediacara biota. Trends Ecol. Evol. 24, 31–40.
Xu, L., Lehmann, B., Mao, J., Qu, W., Du, A., 2011. Re-Os age of polymetallic Ni-Mo-PGE-Au mineralization in early Cambrian black shales of South China-a reassessment. Econ. Geol. 106, 511–522.
Yeasmin, R., Chen, D., Fu, Y., Wang, J., Guo, Z., Guo, C., 2017. Climatic-oceanic forcing on the organic accumulation across the shelf during the Early Cambrian (Age 2 through 3) in the mid-upper Yangtze Block, NE Guizhou, South China. J. Asian Earth Sci. 134, 365–386.
Yin, R.S., Feng, X.B., Hurley, J.P., Krabbenhoft, D.P., Lepak, R.F., Hu, R.Z., Zhang, Q., Li, Z.G., Bi, X.W., 2016. Mercury isotopes as proxies to identify sources and environmental impacts of mercury in sphalerites. Sci. Rep. 6, 18686.
Yin, R.S., Xu, L.G., Lehmann, B., Lepak, R.F., Hurley, J.P., Mao, J.W., Feng, X.B., Hu, R.Z., 2017. Anomalous mercury enrichment in Early Cambrian black shales of South China: mercury isotopes indicate a seawater source. Chem. Geol. 467, 159–167.
Zambardi, T., Sonke, J.E., Toutain, J.P., Sortino, F., Shinohara, H., 2009. Mercury emissions and stable isotopic compositions at Vulcano Island (Italy). Earth Planet. Sci. Lett. 277, 236–243.
Zerkle, A.L., Yin, R., Chen, C., Li, X., Izon, G.J., Grasby, S.E., 2020. Anomalous fractionation of mercury isotopes in the Late Archean atmosphere. Nat. Commun. 11, 1–9.
Zheng, W., Gilleaudeaua, G.J., Kah, L.C., Anbar, A.D., 2018. Mercury isotope signatures record photic zone euxinia in the Mesoproterozoic ocean. Proc. Natl. Acad. Sci. USA 115, 10594–10599.
Zhu, M.-Y., Babcock, L.E., Peng, S.-C., 2006. Advances in Cambrian stratigraphy and paleontology: integrating correlation techniques, paleobiology, taphonomy and paleoenvironmental reconstruction. Palaeoworld 15, 217–222.
Zhu, G.Y., Wang, P.J., Li, T.T., Zhao, K., Zheng, W., Feng, X.B., Shen, J., Grasby, S.E., Sun, G.Y., Tang, S.L., Yan, H.H., 2021. Mercury record of intense hydrothermal activity during the early Cambrian, South China. Palaeogeogr. Palaeoclimatol. Palaeoecol. 568, 110294.